

Characteristic investigations on magnetic field and fluid field of a giant magnetostrictive material-based electro-hydrostatic actuator

Proc IMechE Part G:
J Aerospace Engineering
2018, Vol. 232(5) 847–860
© IMechE 2017
Reprints and permissions:
sagepub.co.uk/journalsPermissions.nav
DOI: 10.1177/0954410017696108
journals.sagepub.com/home/pig



Xulei Yang, Yuchuan Zhu and Yongkai Zhu

Abstract

In this study, an integrative giant magnetostrictive material-based electro-hydrostatic actuator (GMEHA) was designed. Firstly, the uniform of magnetic field distribution on giant magnetostrictive material rod was obtained by using finite element method, i.e. the nonuniformity of the axis and radial direction magnetic field intensity were less than 3% and 0.05%, respectively. Secondly, the flow rate model through the reed valve model was established in COMSOL Multiphysics software, and the relevant properties of reed valves were studied. Thirdly, the dynamic mathematical model of GMEHA was systematically established based on the operational principles of the GMEHA, accordingly, and the simulation model of GMEHA was built in Matlab/Simulink. Finally, the model and simulation results were subsequently verified with the experimental data, which indicates the effective output stroke of the designed GMEHA reached 70 mm, and the maximum no-load output flow was 0.85 L/min at approximately 250 Hz with the best working frequency; the blocked force was nearly 120 N. These results demonstrated the accuracy of the theoretical model and provided a foundation for the design and optimization of the GMEHA.

Keywords

Giant magnetostrictive actuator, electro-hydrostatic actuator, mathematical model, output flow

Date received: 6 June 2015; accepted: 14 January 2017

Introduction

Hydraulic cylinders can provide high force and large displacement, which have been the actuator choice for most aerospace, automotive, and robotic applications. However, a major drawback in the use of the conventional hydraulic actuators is the need for a separate hydraulic power unit equipped with large electric motors and hydraulic pumps that send the high-pressure hydraulic fluid to the actuators through hydraulic lines.^{1–6}

This idea “more-electric aircraft” (MEA) in which the electrical, hydraulic, and pneumatic secondary power systems are combined into a single, electrical system have been a trend in the aerospace industry,^{5,6} which eliminates the need to generate and distribute the hydraulic power; it also reduces the weight and maintenance requirements while improving reliability.^{7–10} To realize these improvements, there is a need to develop new actuators to replace the function of the centralized hydraulic components; accordingly, smart material electro-hydrostatic actuators (SMEHAs) can be used to do this work.^{5,7,11}

Recently, substantial research has been completed on the development of electro-hydrostatic actuators (EHAs) driven by various smart materials as follows:^{5,12} Konishi et al.¹³ in 1993 developed one of the first reported hybrid hydraulic actuators. The maximum output power of the piezoelectric stack-based actuator was 34 W at a working frequency of approximately 300 Hz and a static bias pressure of 3 MPa. A piezohydraulic actuator was developed by Tang et al.¹⁴ and was applied to the active vibration control of rotor dynamic systems. Gerver et al.¹⁵ developed a magnetostrictive material-based hybrid actuator, which obtained high flow by employing stroke amplification, as the test showed,

College of Mechanical and Electrical Engineering, Nanjing University of Aeronautics and Astronautics, Nanjing, PR China

Corresponding author:

Yuchuan Zhu, College of Mechanical and Electrical Engineering, Nanjing University of Aeronautics and Astronautics, 29 Yudao St., Nanjing 210016, PR China.

Email: meeyczhu@nuaa.edu.cn

the no-load output flow of actuator was $30 \text{ cm}^3/\text{s}$ at 35 Hz the input frequency; however, its output power was only 0.3 W. Mauck and Lynch¹⁶ developed a piezoelectric stack-based device in which the output power was approximately 4.9 W, while the blocked force approached 271.7 N. The working frequency of this device was limited under 60 Hz due to the cost of a large loss tangent (high hysteresis) without a cooling system. Lee et al.¹⁷ developed a piezoelectric-hydraulic actuator that could rectify fluid flow by using active unimorph disk valves. Testing showed that the flow rate was $3.4 \text{ cm}^3/\text{s}$, the pump specific power density was 12 W/kg, and a stall pressure of 8.3 MPa occurred at the output frequency of 100 Hz. Tan et al.¹⁸ developed a piezohydraulic actuation system with active valves. The test results showed that the system performance could reach approximately 140 Hz, and the valve timing was important to the system performance. Rupinsky and Dapino¹⁹ designed an EHA using magnetostrictive material. This EHA show a blocked pressure of 7.6 MPa and an output flow rate of $2.2 \text{ cm}^3/\text{s}$ at 160 Hz. John et al.²⁰ performed a comparison of actuator performance with different smart materials (PMN and Terfenol-D). In each case, the active material has the same size. While an identical maximum output power of 2.5 W was obtained for the Terfenol-D and PMN-based devices, the latter was found to be significantly more efficient (7% vs. 0.5%) and had a higher no-load output flow rate ($26 \text{ cm}^3/\text{s}$ vs. $24 \text{ cm}^3/\text{s}$).²⁰ Chaudhuri et al.²¹ compared two different lengths of Terfenol-D rods (51 mm and 102 mm) within an actuator system. They were both reported to have similar performance. The maximum no-load output velocity was 84 mm/s with a 51 mm long rod and 88 mm/s with a 102 mm long rod, both noted at an approximate 325 Hz pumping frequency, while the blocked force was roughly 89 N. Kim and Wang²² designed a piezoelectric-hydraulic pump (PHP) for automotive transmissions. To minimize the size, complexity, and weight of a piezoelectricity-based valve system, two passive reed valves were fabricated to achieve the functions of a one-way valve. The maximum flow rate was $19 \text{ cm}^3/\text{s}$ at a 230 Hz pumping frequency under an accumulator pressure of 0.4 MPa, and the peak deadhead pressure was 0.55 MPa. Chaudhuri and Wereley²³ developed a hybrid electrostrictive hydraulic actuator driven by the single-crystal electrostrictive material. The test results showed that the maximum actuator velocity was 330 mm/s and the corresponding flow rate was $42.5 \text{ cm}^3/\text{s}$; the blocked force of the actuator was 63 N. Larson and Dapino²⁴ developed a magnetostrictive-hydraulic actuator. Testing of the system showed that the output performance increased with a frequency up to a peak unloaded flow rate of $100 \text{ cm}^3/\text{s}$ at 1200 Hz, which is a 100–500% increase over previous state-of-the-art systems. A blocked differential pressure of 12.1 MPa was measured, resulting in a power capacity of 310 W,

100 W higher than the previously reported values. Xuan et al.²⁵ developed a piezoelectric-hydraulic actuator, and the test results showed that the maximum blocked force was 346 N and the no-load velocity was 101 mm/s, resulting in a maximum output power of 8.74 W at 1000 V applied voltage and 250 Hz pumping frequency. However, the application of the device was limited due to the high voltage.

Various smart materials have been developed for potential use in aerospace, automotive, and robotic applications.^{1–3,5,7,10,11,26–28} However, piezo-stacks generate significant heat mainly due to the hysteresis losses that can deteriorate their performance and permanently damage the piezomaterial at high driving frequencies. In contrast, a giant magnetostrictive material (GMM) are more robust than piezo-stacks, especially at high temperatures, while offering approximately the same bandwidth and higher maximum induced strain compared with the piezoelectric stacks.

As a subset of EHAs, a giant magnetostrictive material-based electro-hydrostatic actuator (GMEHA) can create a compact structure and a power-by-wire system by collocating the output hydraulic cylinder with its supply pump. The system is a self-contained unit, thus eliminating the weight and associated maintenance requirements of a centralized hydraulic pump, fluid lines, and control valves.^{2,5,6,12,27}

To make a GMEHA work in optimum driving conditions, several key design parameters must be considered in this paper. First of all, the magnetic field distribution was studied according to the uniformity analysis of magnetic field distribution on the GMM rod. Secondly, based on the principle of interaction between the fluid and the reed structure, the flow rate model through the reed valve have been built and the relevant properties were studied to provide the basis for optimizing the main structure parameters of the reed valves. Finally, a precise dynamic mathematical model of GMEHA was established considering the dynamic characteristic of reed valves and the inertia of fluid. The dynamic output performance of GMEHA was analyzed and showed good consistency with the experimental results.

Structure and working principle

Figure 1 shows the GMEHA designed for this study. The GMEHA consists of four separate parts: a pumping section, a hydraulic cylinder, an accumulator, and the tubing and fittings (as shown in Figure 2).

As the power provider of GMEHA, the pumping section is driven by an alternating magnetic field, which comes from the alternating current. The magnetic field intensity flux generated from the current can form a closed magnetic flux through the GMM rod and magnetizers, which consists of a bottom cap, a pump body, a top cap, and an output shaft. The GMM rod is eventually magnetized, and it can

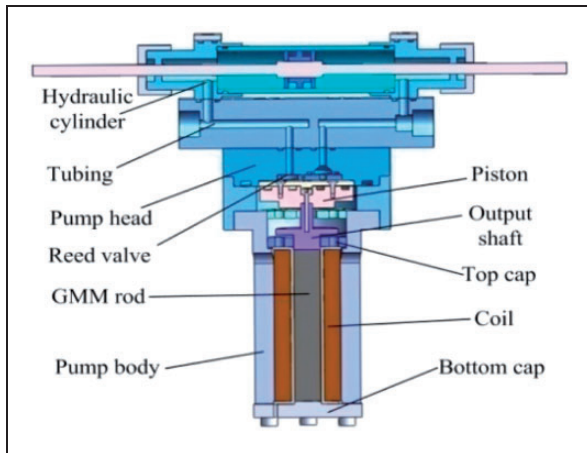


Figure 1. Sectional view of the GMEHA assembly.

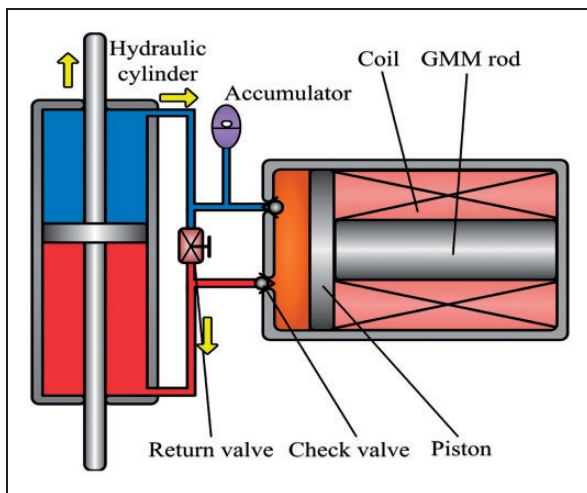


Figure 2. Schematic diagram of the GMEHA.

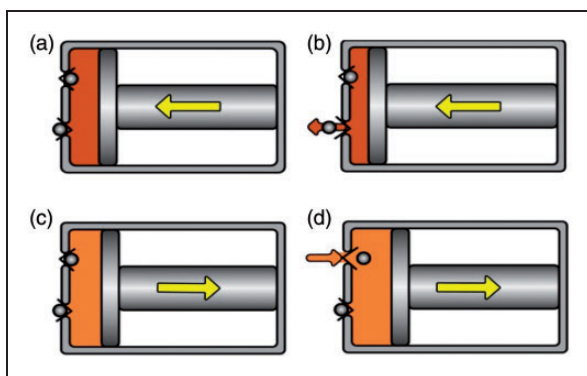


Figure 3. Operational principle of the GMEHA.

produce displacement and drive the piston to constantly move back and forth. The pump chamber can absorb or drain fluid due to the volumetric change. This can provide output power using the frequency rectification principle, which is based on the passive unidirectional reed valves housed inside the pump head.

As shown in Figure 3, the GMEHA operation can be divided into four stages: compression, exhaust, expansion, and intake.^{25,28}

1. Compression: With the sinusoidal electricity supply, expansion of the GMM rod pushes the hydraulic fluid in the closed pump chamber, resulting in the pressure increase inside the chamber.
2. Exhaust: At this stage, the outlet valve opens due to the pressure difference; fluid then begins to flow into the outlet tube, and the pressure builds in the high-pressure-driven side of the output cylinder and results in motion of the output shaft.
3. Expansion: This stage is similar to the compression stage; however, the stack begins to reduce with the decreasing applied field, causing the pressure drop in the pumping chamber.
4. Intake: At this stage, the pressure in the pump chamber drops further to crack open the intake reed valve and to allow fluid to flow from the low-pressure-driven side of the output cylinder back into the chamber.

These four stages are repeated during each pump cycle and result in a net mass flow rate out of the pump through the outlet tube and an equivalent mass flow rate into the pump through the inlet tube.

Finite element analysis

To optimize the GMEHA structure and maximize its output performance, the key components of the GMEHA are analyzed using COMSOL Multiphysics, which includes the magnetic field and fluid–solid coupling field between fluid and reed valve.

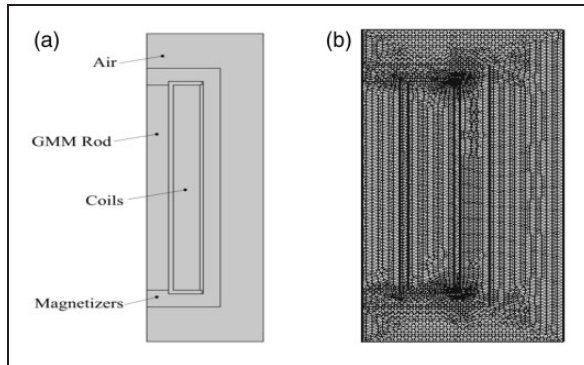
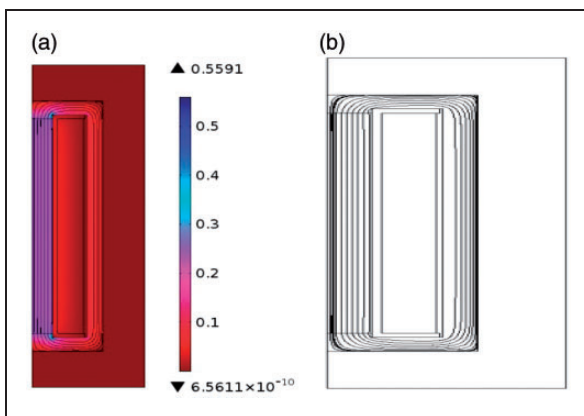
Finite element analysis of the magnetic field

The output performance of the GMM rod depends on the strength and uniformity of the magnetic field, and the magnetic field strength depends on the input current. So, it is necessary to analyze the magnetic field uniformity of giant magnetostrictive actuator (GMA), which include GMM rod, coil, bottom cap, pump body, and output shaft as shown in Figure 1 by the finite element method, and the simulation parameters are shown in the Table 1. Mesh type is trilateral and mesh is shown in Figure 4.

According to Figure 5, the magnetic flux line can form a closed magnetic flux loop through the GMM rod and magnetizers. To achieve more accurate conclusions, the axial and the radial magnetic field intensity are analysed in the next step under the condition of input current $i = 3 \text{ A}$ and coil turns $N = 1000$. The magnetic field intensity distribution in the axis of the GMM rod under various coil lengths (74 mm, 80 mm, 86 mm) is shown in Figure 6, and Figure 7 shows the uniformity of the radial magnetic field intensity at

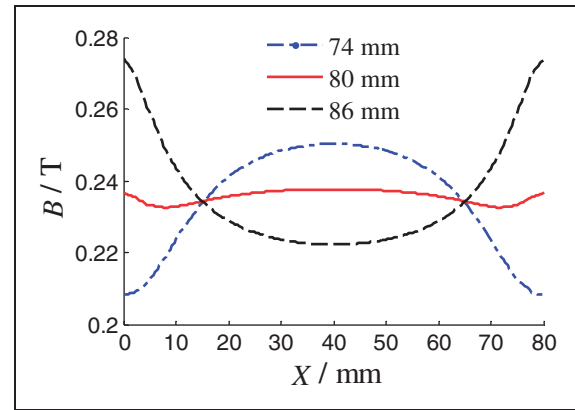
Table 1. Simulation parameters.

Material type	Relative permeability	Electric conductivity	Relative permittivity
GMM	5	1.667×10^6	1
DT4C	11947	10^7	1
Air	1	0	1
Nylon	1	0	1

**Figure 4.** Finite element model of GMA: (a) configuration; (b) mesh.**Figure 5.** Finite element analysis result of GMA: (a) magnetic flux; (b) magnetic flux line.

different GMM rod axis positions (10 mm, 20 mm, 30 mm, 40 mm).

As shown in Figure 6, the magnetic field intensity on the axis of the GMM rod presents concave distribution such that the middle is lower than both ends. This occurs when length of the coil is less than that of the GMM rod. The distribution is opposite, however, when the length of the coil is greater than that of the GMM rod. The magnetic field intensity presents fine uniformity when length of the coil is closed to that of the GMM rod. By calculating the average magnetic field intensity of the three situations, the results are closed.

**Figure 6.** The magnetic field intensity distribution on the axis of the GMM rod.

According to Figure 6, the radial magnetic field intensity of the GMM rod changes little in the different axial positions, but it presents good uniformity.

The numerical simulation method for magnetic field can be used to reduce the nonuniformity of the magnetic field. The discrete form of the nonuniformity formula is given by

$$\delta_B = \frac{\sum_{i=1}^n |B_i - \bar{B}|}{n\bar{B}} \quad (1)$$

where n is the number of the analysis points.

Based on equation (1), the calculated results show that the nonuniformity of the axis and radial direction magnetic field intensity are less than 3% and 0.05%, respectively. In summary, the radial magnetic field intensity is more uniform than the axial magnetic field intensity. The analysis of the magnetic field intensity uniformity should mainly focus on the axis magnetic field.

The numerical simulation of the magnetic field is completed for magnetizers (on other components except for the GMM rod) with different materials on the magnetic circuit, of which the relative permeability can respectively reach 100, 300, 1000, 10000. The relationship between the distribution of the axial magnetic field intensity and the relative permeability of magnetizers, based on calculations, is shown in Figure 8.

As shown in Figure 8, the material of the magnetizers has a small influence on the uniformity of the magnetic field intensity, but the magnetic field intensity on the axis of the GMM rod will increase along with the improvement of the relative permeability of the magnetizers on the magnetic circuit. The increasing trend will not be obvious when the magnetic field intensity reaches a certain value.

According to the above analysis, the optimization should mainly focus on the uniformity of the magnetic field and the magnetic energy utilization for the magnetic field of the GMEHA. Therefore, it should satisfy the following: the length of the driving coil is close to

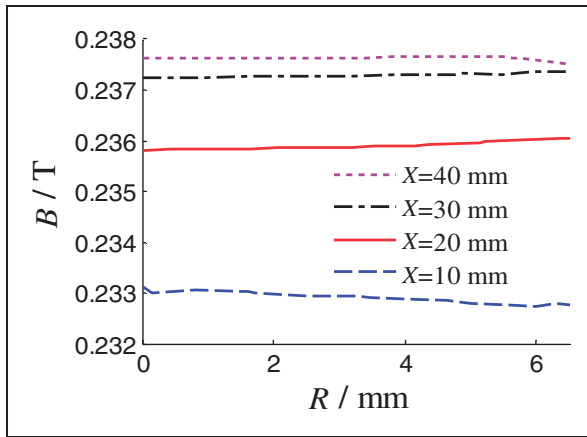


Figure 7. The magnetic field intensity distribution in the radial direction of the GMM rod.

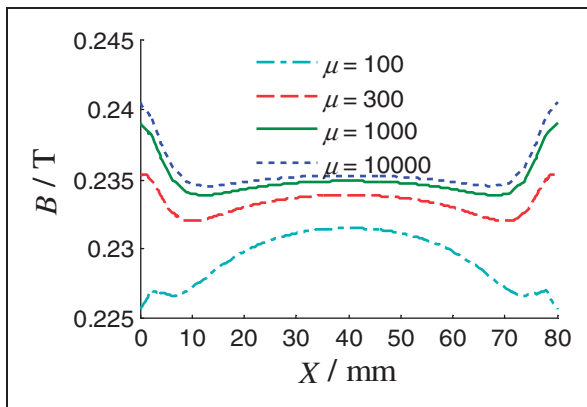


Figure 8. Magnetic field intensity under various magnetizer materials.

that of the GMM rod, and the relative permeability of the magnetizers on the magnetic circuit, except for the GMM rod, is relatively large.

The analysis results of the magnetic field intensity uniformity show that the axis of the magnetic field should be focused in the first place, as a consequence, we design the length of the excitation coil to be 80 mm. The analysis results of magnetizers in GMA with different materials show that a GMA has a good uniformity of the magnetic field when the permeability of magnetizers is greater than 10,000. As a consequence, we design the magnetizers' relative permeability value to be 11,947.

Flow analysis of the reed valve

The reed valves can rectify the fluid flow from the pump chamber in the GMEHA. The response speed of the reed valves directly affects the working bandwidth of the GMEHA. There are also pressure losses due to flow through the reed valves. The fluid flow through the reed valves is an extremely complex phenomenon involving the interaction between the fluid and the reed structure. To optimize the reed valve

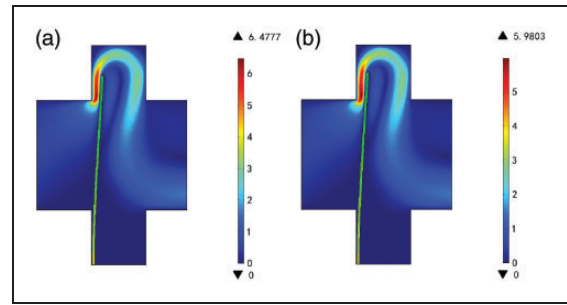


Figure 9. Flow with a 0.10-mm-thick reed valve: (a) pressure = 25 kPa; (b) pressure = 30 kPa.

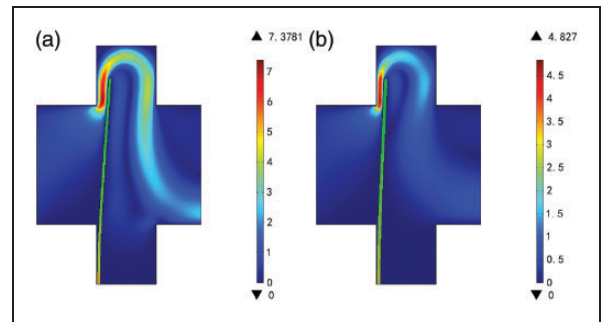


Figure 10. Flow with a 35 kPa pressure reed valve: (a) thickness = 0.10 mm; (b) thickness = 0.12 mm.

structure and create a more accurate reed valve model, the fluid–structure interaction module in COMSOL Multiphysics software is used to analyze the influential factors of the valve performance.

Steady flow analysis of reed valves. The behavior of different differential pressures as well as different thicknesses and lengths of reed valves are shown in the flow study in Figures 9 to 11.

As shown in Figures 9 to 11, the differential pressure, the thickness, and the length of the reed valve have an effect on the output flow through the valve.

To achieve more effective and accurate analysis results, the opening displacement change of the reed valve is analyzed (Figures 12 to 14).

As shown in Figure 12, the pressure difference is mainly manifested in the impact on the opening displacement of the reed valve. The response of the reed valve is not sensitive at the beginning of the deformation because the effective area that the pressure acts on is smallest before the reed valve deformation. The effective area becomes larger with the deforming process of the valve, and the force acting on the reed valve is also increasing with enlargement of the effective area. The response speed of the reed valve is fastest when the effective area is largest.

As shown in Figure 13, the reed valve response speed is improved with the increase of the reed valve

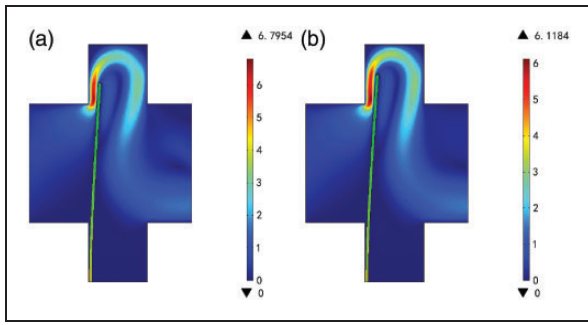


Figure 11. Flow with a 30 kPa pressure and 0.10-mm-thickness reed valve: (a) length = 6.7 mm; (b) length = 7.0 mm.

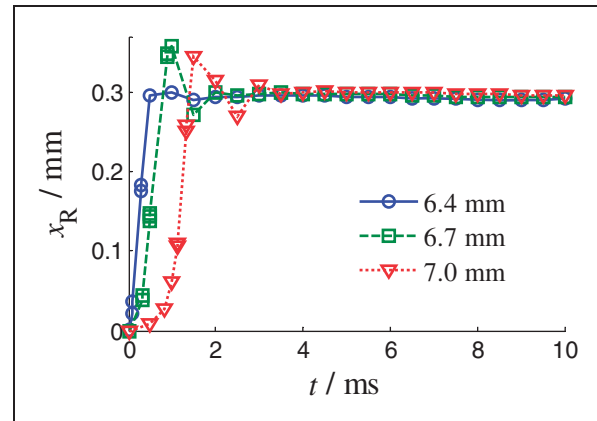


Figure 14. Reed valve displacement under various lengths.

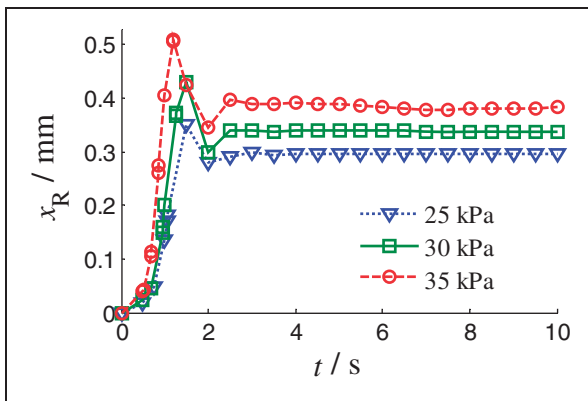


Figure 12. Reed valve displacement under various pressures.

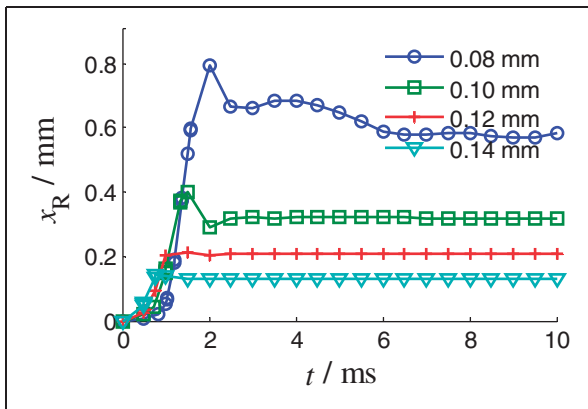


Figure 13. Reed valve displacement under various thicknesses.

thickness, but the opening displacement is decreased within a certain degree. The reed valve disturbance will appear and steady state will not be easily reached if the thickness of the reed valve is too thin. The fluid resistance is too large due to the small opening displacement when the thickness of the reed valve is too large. The reed valve thickness is the main influence on the stiffness of the valve. Hence, the reed valve should not only maintain suitable rigidity, but it should also have suitable elasticity.

As shown in Figure 14, the geometric size of the reed valve has a large impact on the response speed of the valve. The reed valve with a shorter length will have a faster response speed, and the response reaches steady state much faster. So, to improve the bandwidth of the GMEHA, the length of the reed valve should be as short as possible.

As the designed diameter of inlet and outlet port in GMEHA is 4 mm, the length of reed valve should be a little greater than 4 mm; accordingly, we make a simulation research on the dynamic opening displacement of reed valves by 6.4 mm, 6.7 mm, and 7 mm, based on the simulation results and consideration for realizing the manufacture, the actual value of reed valve is 6.7 mm in GMEHA.

Dynamic flow analysis of the reed valve. The transient behavior of the reed valve is strongly dependent on the time-varying pressure difference across the valve port. This dynamic behavior was also simulated using COMSOL Multiphysics. The pressure (δP) at the inlet boundary is a varying parameter, while the outlet boundary is maintained at zero pressure. The pressure change δP and the opening displacement x_R of the reed valve under various frequencies are shown in Figures 15 to 18.

As shown in Figures 15 to 19, the response lag of the reed becomes more obvious with the driving frequency increase. This can lead to valve float, which means the valve fails to close completely between cycles and causes back flow through the pump chamber at high driving frequency. Additionally, the maximum opening displacement of the reed valve also decreases with the driving frequency increase, in this way, a less opening displacement will cause a higher pressure loss.

According to the above analysis, the reed valve should be selected with a thickness of 0.1–0.2 mm, and it should be constructed stainless steel or beryllium bronze, which both have good elasticity and suitable stiffness. The geometric size of reed valve should also be most suitable to only cover the valve port.

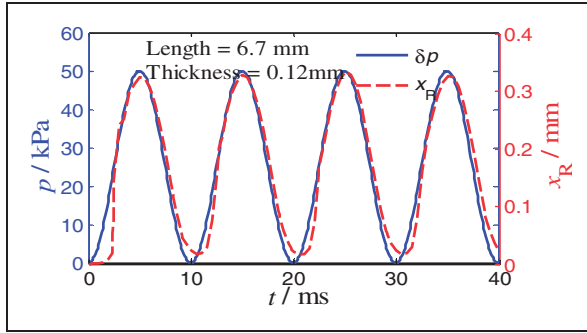


Figure 15. Transient behavior of reed valve at 100 Hz.

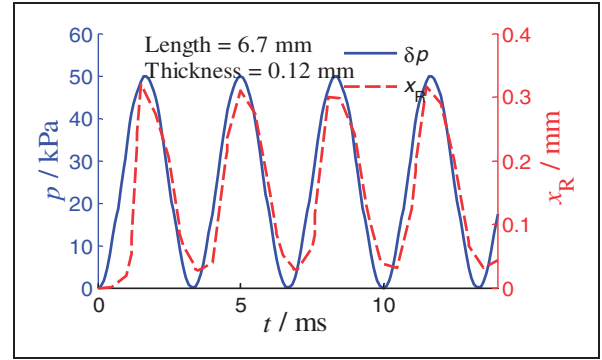


Figure 18. Transient behavior of reed valve at 300 Hz.

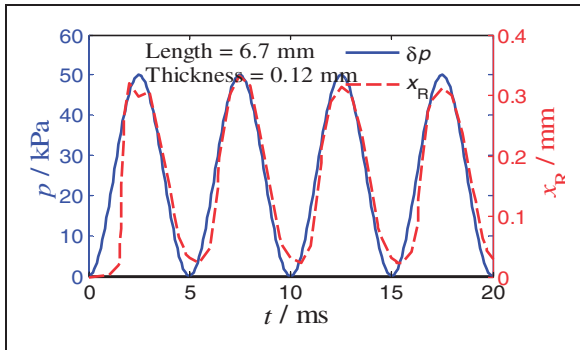


Figure 16. Transient behavior of reed valve at 200 Hz.

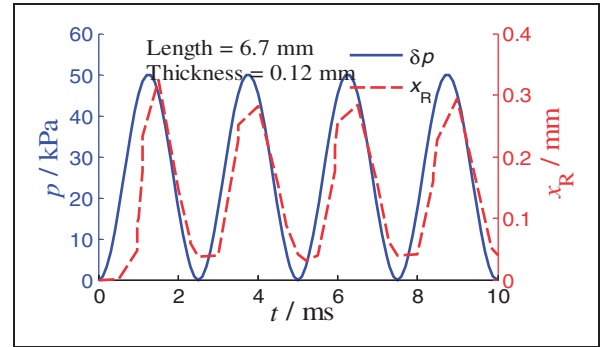


Figure 19. Transient behavior of reed valve at 500 Hz.

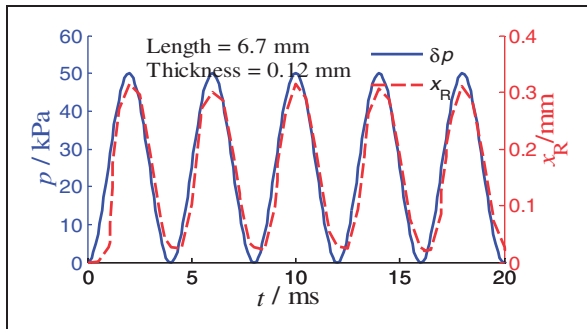


Figure 17. Transient behavior of reed valve at 250 Hz.

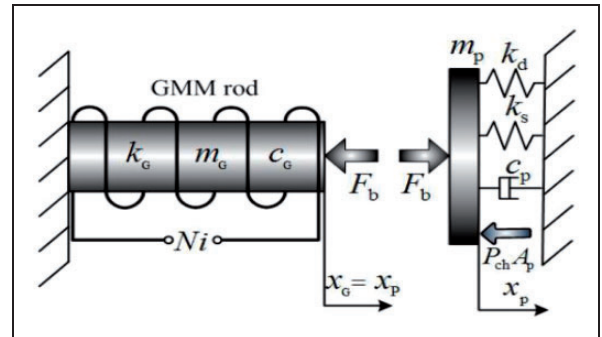


Figure 20. SDOF model for GMA.

GMEHA model

The structure of GMEHA can thus be optimized based on the previous analysis. Presently, the theoretical model is created based on the structure of the GMEHA.

GMEHA theoretical model consists of the driving model, the pump chamber model, the reed valve model, the fluid tubing model, and the cylinder output model according to different functions.

GMEHA driving model

GMA provides the energy for the entire system. Firstly, the GMA mathematical model should be established.

As shown in Figure 20, based on the principle of structural dynamics, the motion equation of the piston is written by considering it as a single degree of freedom (SDOF) system as follows

$$\left(m_p + \frac{m_G}{3}\right)\ddot{x}_p + (c_p + c_G)\dot{x}_p + (k_d + k_s + k_G)x_p = F_G - p_{ch}A_p \quad (2)$$

where m_p and m_G are the mass of piston and the GMM rod, respectively, c_p and c_G are the damping constant of piston and GMM rod, respectively, k_d , k_s , k_G are the various metal diaphragm stiffnesses, spring and GMM rod, respectively, p_{ch} is pressure of the

pump chamber and A_p is the cross-sectional area of the piston. F_b is the force acting on the GMM rod that prevents it from reaching its free strain. The output force can be calculated on the condition that the eddy be considered as follows²⁹

$$F_G = \delta \left(Ni + \frac{x_p}{d_{33}} \right) / d_{33} R_m \quad (3)$$

where δ , d_{33} , R_m , N are the eddy constant ($\delta = 1$ when the eddy is not considered), the piezomagnetic coefficient, the magnetic reluctance, and the coil turns, respectively. The eddy constant δ is given by

$$\delta = \exp\left(-\frac{\rho_G}{\vartheta}\right) \quad (4)$$

where ρ_G is the radius coordinate of the GMM rod (the value found by extroversion, the outermost value is 0), and ϑ is the skin depth. The skin depth is calculated by²⁹

$$\vartheta = \sqrt{\frac{2}{\omega\gamma\mu_0\mu_G}} \quad (5)$$

where ω , γ , μ_0 , μ_G are the excitation angular frequency, the conductivity of the GMM, the permeability of the vacuum, and the relative permeability, respectively.

GMEHA pump chamber model

Compressibility of the fluid is considered before establishing the model.

As shown in Figure 21, the effective bulk modulus of the fluid with entrained air will observably decline.³⁰ The effective bulk modulus of the fluid has a large impact on the output performance of the GMEHA. Therefore, it is essential to improve the effective bulk modulus of the fluid using an accumulator, which provides the bias pressure.

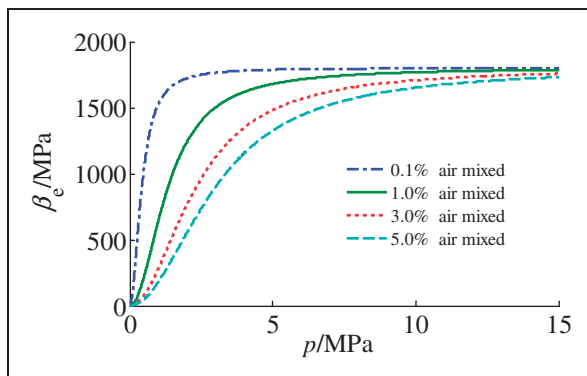


Figure 21. Fluid bulk modulus under various mixed proportion air.

Considering an enclosed volume of fluid, there is no net mass inflow or outflow²⁸

$$\frac{dm}{dt} = 0 \Rightarrow \frac{d(\rho V)}{dt} \Rightarrow \dot{\rho} = -\rho \frac{\dot{V}}{V} \quad (6)$$

Equation (6) indicates that the instantaneous fluid density is related to the change of fluid volume in the enclosed volume. Considering the bulk modulus of fluid, the following equation can be obtained

$$dp = -\beta_e \frac{dV}{V} \Rightarrow \frac{V}{V_0} = \exp\left(-\frac{p}{\beta_e}\right) \quad (7)$$

The effective bulk modulus of fluid, β_e , can be calculated as follows³¹

$$\beta_e = \left[\frac{V_f/V_a + p_a/p_{acc}}{V_f/V_a + \beta_f \cdot p_a/p_{acc}^2} \right] \cdot \beta_f \quad (8)$$

where β_f is the bulk modulus of fluid without any air; V_a and V_f are the volume of entrained air and the fluid volume, respectively; p_a and p_{acc} is the atmospheric pressure and the pressure provided by the accumulator, respectively.

Based on equations (7) and (8), the effective bulk modulus of the fluid is greatly improved due to bias pressure provided by the accumulator. The fluid volume is relatively steady with the pressure change. According to equation (6), the density was relatively equivalent when the volume of fluid slightly changed. To simplify the model, the density is deemed as a constant when considering the accumulator in the calculations.

As shown in Figure 22, the corresponding pressure change rate inside the chamber can be obtained by applying equation (7), as shown below^{2,7}

$$\dot{p}_{ch} = \beta_e \frac{A_p \dot{x}_p + Q_{in} - Q_{out} - Q_{loss}}{A_p(h - x_p)} \quad (9)$$

where Q_{in} , Q_{out} , Q_{loss} , h are the inlet flow rate, the outlet flow rate, loss of flow rate, and the height of the pump chamber, respectively.

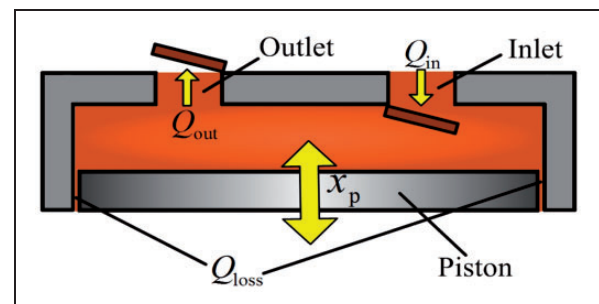


Figure 22. Schematic of fluid flow in the pump chamber.

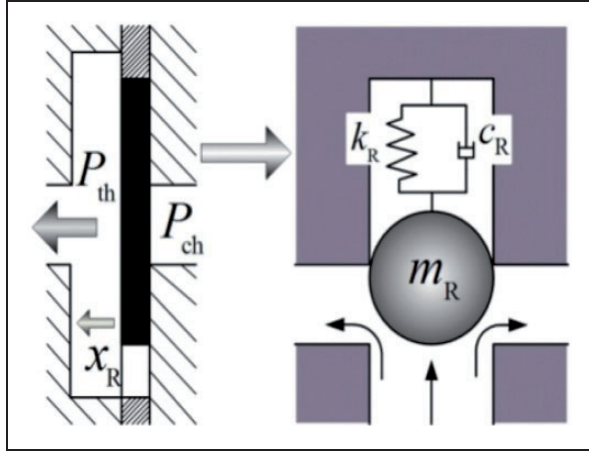


Figure 23. SDOF model for reed valves.

GMEHA reed valve model

The reed valve dynamics can be described as a SDOF lumped parameter model because the nominal operation frequency is lower than the bandwidth of the reed valve and will not excite the higher order modes of the reed valve. The stiffness of the reed valve is approximately determined by the results of the finite element simulation.

As shown in Figure 23, the governing equation of reed valves opening displacement can be written as⁷

$$\begin{cases} \text{outlet} : m_R \ddot{x}_{Ri} + c_R \dot{x}_{Ri} + k_R x_{Ri} = A_R (p_{ch} - p_{th}) \\ \text{inlet} : m_R \ddot{x}_{Ro} + c_R \dot{x}_{Ro} + k_R x_{Ro} = A_R (p_{tl} - p_{ch}) \end{cases} \quad (10)$$

where m_R , c_R , k_R are the equivalent mass, the damping, and the stiffness of the reed valve, respectively; x_{Ri} and x_{Ro} are the opening displacement of the reed valve inlet and outlet, respectively; A_R is the effective area of the reed valve; p_{th} is the pressure that prevents the reed valve from opening on the high pressure side; p_{tl} is the pressure that opens the reed valve on the low side. The equivalent mass of the reed valve can be written as³²

$$m_R = 2.75 \left(\rho_R V_R + \frac{\pi}{4} \rho f L_R W_R \right) \quad (11)$$

where ρ_R is the reed valve density, V_R is the reed valve volume, ρ is the fluid density, f is the driving frequency, and L_R and W_R are the length and width of the reed valve.

Once the pumping pressure is generated by stroking the GMM rod, the outlet flow rate and the inlet rate through the two reed valves can be expressed by the orifice equations as follows⁷

$$Q_{out} = \text{sgn}(\Delta p_{ch-th}) \cdot c_d w \cdot x_{Ro} \sqrt{\frac{2}{\rho} (p_{ch} - p_{th})}$$

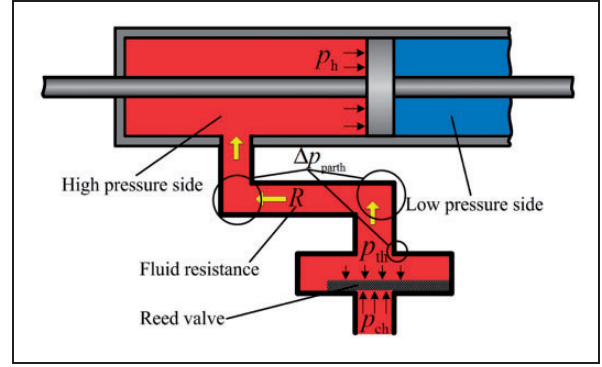


Figure 24. Schematic of the fluid flow in the high-pressure side.

$$x_{Ro} = \begin{cases} x_{Ro} , & x_{Ro} > 0 \\ 0 , & x_{Ro} \leq 0 \end{cases} \quad (12)$$

$$\begin{aligned} Q_{in} &= \text{sgn}(\Delta p_{tl-ch}) \cdot c_d w \cdot x_{Ri} \sqrt{\frac{2}{\rho} (p_{tl} - p_{ch})} , \\ x_{Ri} &= \begin{cases} x_{Ri} , & x_{Ri} > 0 \\ 0 , & x_{Ri} \leq 0 \end{cases} \end{aligned} \quad (13)$$

where c_d is the discharging flow coefficient and w is the orifice area gradient. The backward flow can be eliminated in equations (12) and (13).

GMEHA fluid tubing model

As shown in Figure 24, the fluid flows from the pump chamber to the high-pressure side of the hydraulic cylinder. This process causes the movement in the output shaft of the hydraulic cylinder.

Based on the Bernoulli's equation, the pressure loss across any section can be accounted for as follows

$$p_{ch} + \rho \frac{\alpha_1 v_{th}^2}{2} = p_h + \rho \frac{\alpha_2 \dot{x}_L^2}{2} + p_a + p_{lossh} \quad (14)$$

Equation (14) presents the relationship between the pressure and energy per unit volume of fluid, where v_{th} is the outlet flow velocity of the pump chamber, α_i is the correction coefficient, p_a is the pressure drop caused by the fluid inertia, and p_{lossh} is total pressure loss from the pump chamber to the high side of the hydraulic cylinder. p_a and p_{lossh} are as shown in the following equations

$$p_a = \rho \int_0^{l_{th}+l_L} \frac{\partial}{\partial t} (\alpha_3 v) dl \quad (15)$$

$$p_{lossh} = \Delta p_{th} + \Delta p_{parth} \quad (16)$$

where l_{th} and l_L are the tubing length and the effective length of the hydraulic cylinder, respectively, Δp_{th} is

the frictional pressure loss caused by the fluid viscosity, Δp_{parth} is the partial pressure caused by turning.

The frictional pressure loss caused by the fluid viscosity can be written as

$$\Delta p_{\text{th}} = Q_{\text{out}}(l_{\text{th}}R_{\text{th}} + l_{\text{L}}R_{\text{L}}) \quad (17)$$

where R is the viscous resistance of the fluid flow in the tubing per unit length.

The viscous fluid resistance can be calculated from the Hagen–Poiseuille solution for laminar flow through a circular tube²

$$\Delta p_{\text{lamimar}} = \frac{128\nu}{\pi D^4} LQ \Rightarrow R = \frac{8\pi u}{A^2} \quad (18)$$

where u is the dynamic viscosity of the fluid, and A is the cross-sectional area of the tubing.

Partial pressure loss occurs when the fluid flows across the partial change of tubing. It can be written as

$$\Delta p_{\text{parth}} = \frac{\rho}{2} \sum_{i=1}^N \left(\xi_{\text{thi}} \frac{Q_{\text{out}}^2}{A_{\text{thi}}^2} \right) \quad (19)$$

where ξ_{thi} is the resistance coefficient.

As shown in Figure 25, a similar process occurs on the fluid flowing from the accumulator to the pump chamber.

The process (as shown in Figure 25) can be calculated by the following equations

$$p_{\text{acc}} + \rho \frac{\alpha_4 v_{\text{acc}}^2}{2} = p_{\text{ch}} + \rho \frac{\alpha_5 v_{\text{tl}}^2}{2} + \rho \int_0^{l_{\text{tl}}} \frac{\partial}{\partial t} (\alpha_6 v) dl + p_{\text{lossl}} \quad (20)$$

$$p_{\text{lossl}} = \Delta p_{\text{tl}} + \Delta p_{\text{partl}} \quad (21)$$

$$\Delta p_{\text{tl}} = Q_{\text{in}} l_{\text{tl}} R_{\text{tl}} \quad (22)$$

$$\Delta p_{\text{partl}} = \frac{\rho}{2} \sum_{i=1}^N \left(\xi_{\text{tli}} \frac{Q_{\text{in}}^2}{A_{\text{tli}}^2} \right) \quad (23)$$

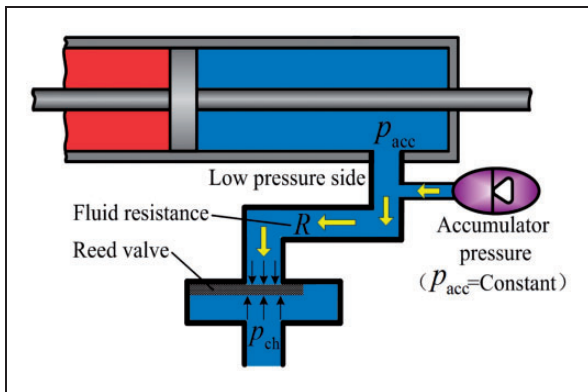


Figure 25. Schematic of the fluid flow in the low-pressure side.

where v_{acc} is the inlet flow velocity of the pump chamber, and p_{lossl} is the total pressure loss of the process in which the fluid flows from the accumulator to the chamber.

GMEHA cylinder output model

The output model of the hydraulic cylinder mainly shows that the pressure difference on both sides of the cylinder piston push the cylinder piston to drive the load movement.

As shown in Figure 26, the low-pressure driving side is considered as a constant due to the low accumulator stiffness. Considering the friction between piston and cylinder wall, the equation can be expressed as²

$$m_{\text{L}} \ddot{x}_{\text{L}} + c_{\text{L}} \dot{x}_{\text{L}} = (p_{\text{h}} - p_{\text{acc}}) A_{\text{L}} - F_{\text{f}} - m_{\text{L}} g \quad (24)$$

where m_{L} is the total mass of the output shaft and the load, c_{L} is the piston movement damping, and F_{f} is the friction between the piston and the cylinder wall, which can be written as follows according to the Karnopp model²

$$F_{\text{f}} = \begin{cases} \text{sgn}(v_{\text{L}}) F_{\text{d}} & |v_{\text{L}}| > v_{\text{min}} \\ \text{sgn}(F) \min(F, F_{\text{s}}) & |v_{\text{L}}| \leq v_{\text{min}} \end{cases} \quad (25)$$

where $F = (P_{\text{h}} - P_{\text{l}}) A_{\text{L}} - m_{\text{L}} g$ is the force acting on the piston, F_{d} and F_{s} is the static and dynamic friction in the hydraulic cylinder ($F_{\text{d}} = F_{\text{s}}/3$).

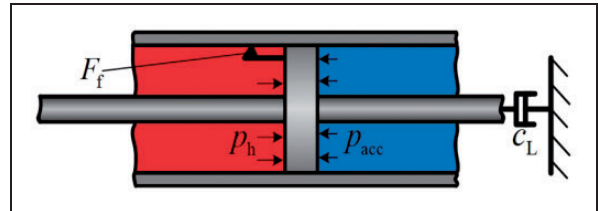


Figure 26. Schematic of the fluid flow in the hydraulic cylinder.

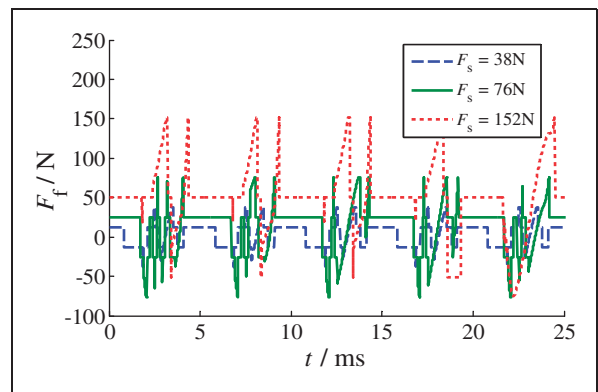


Figure 27. The actual friction in the hydraulic cylinder under various static frictions.

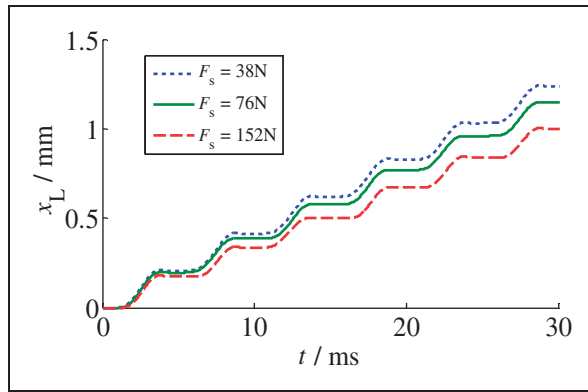


Figure 28. The hydraulic cylinder displacement under various static frictions.

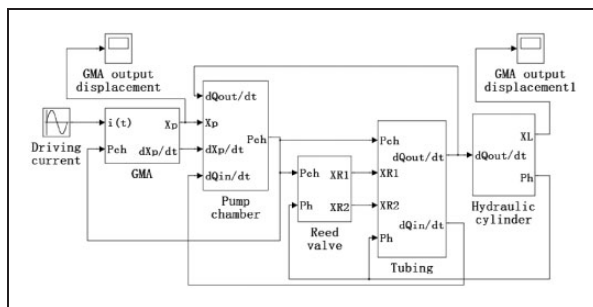


Figure 29. Simulation model of GMEHA.

The friction in the hydraulic cylinder influences the output performance of GMEHA, as shown in Figures 27 and 28, under 200 Hz excitation frequency, with the increase in the static friction F_s . The actual friction F_f in the hydraulic cylinder change alternately between the dynamic friction and the static friction and, accordingly, the output displacement of hydraulic cylinder decreases.

Simulation model

As shown in Figure 29, the simulation model is created in Matlab/Simulink, based on the above theoretical model. Table 2 presents the major parameters of the GMEHA simulation model (various parameter values are from Chaudhuri,² Kim and Wang,⁷ Kim,³¹ and Walters³³).

Experimental investigation

To analyze the experimental data and verify the accuracy of the theoretical model, a test bench was set up to determine the output performance of the GMA (see Figure 29), and another test bench was set up to determine the output performance of the GMEHA (see Figure 30). The output displacements of the GMA and GMEHA are respectively measured using two different types of laser displacement sensors (precision is 0.2 μm and 2.5 μm , respectively;

Table 2. Related parameters of GMEHA.

Name	Unit	Sign	Value
GMM rod radius	mm	r_G	6.5
GMM rod length	mm	h_G	80
GMM rod relative permeability	l	μ_G	5
Permeability of vacuum	H/m	μ_0	$4\pi \times 10^{-7}$
Coil turns	l	N	1000
GMM rod elasticity modulus	GPa	E_G	35
GMM rod damping	$\text{N}\cdot\text{s}\cdot\text{m}^{-1}$	c_G	4.20×10^3
GMM rod mass	kg	m_G	0.084
Piston mass	kg	m_p	0.03
Pump chamber height	mm	h	0.5
Pump chamber radius	mm	r_{ch}	23
Fluid bulk modulus without any air	MPa	β	1800
Orifice area gradient	l	w	3.14×10^{-3}
Fluid density	kg/m^3	ρ	860
The reed valve thickness	mm	h_R	0.15

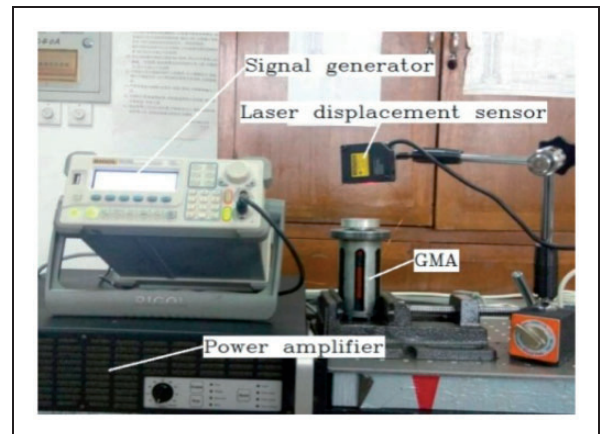


Figure 30. Test bench of the GMA.

measuring range is 1 cm and 12 cm, respectively), a signal generator and a power amplifier that supplies current to the exciting coil of the GMA and the GMEHA. The output force of the GMEHA is measured by applying different load weights.

The test conditions and parameters are as follows: the DC input current is 3 A, the AC amplitude is 3 A, and there are 1000 turns per coil.

GMA output displacement experiment

As shown in Figure 30, a signal generator and power amplifier provide the driving current with adjustable frequency, adjustable amplitude. A laser displacement sensor with a sampling frequency of 10 kHz measures the output displacement of the actuator.

The model results and experimental data of the GMA output displacement with the excitation frequencies of 200 Hz and 350 Hz are shown in Figures 31 and 32.

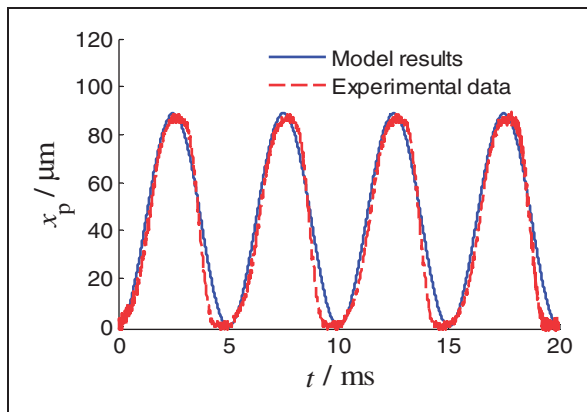


Figure 31. GMA output displacement at 200 Hz.

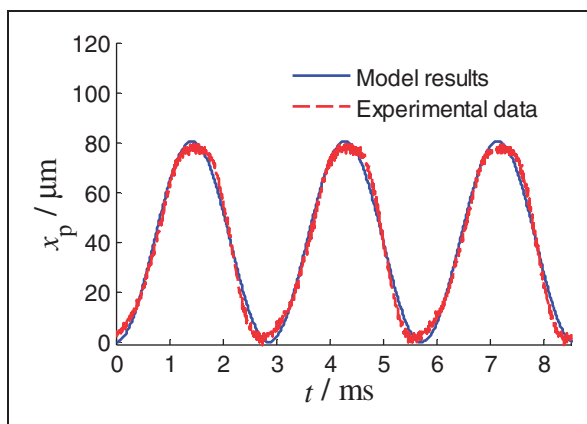


Figure 32. GMA output displacement at 350 Hz.

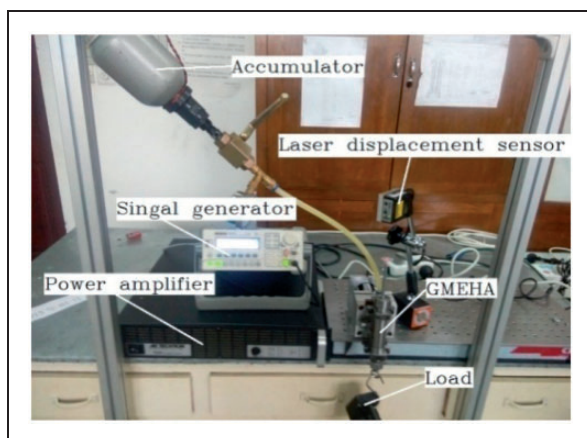


Figure 33. Test bench of the GMEHA.

As shown in Figures 31 and 32, the experimental data of GMA output displacement match the model results.

GMEHA output performance experiment

As shown in Figure 33, the GMEHA output performance test bench is set up according to the GMEHA

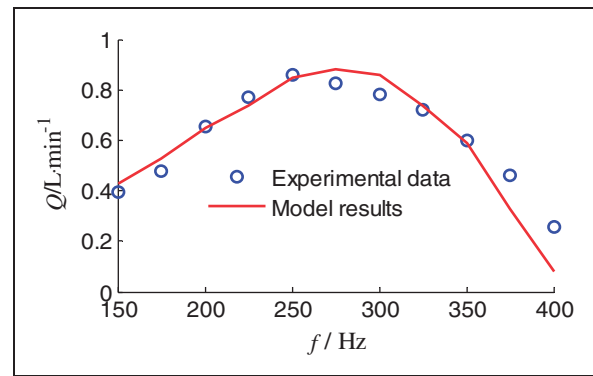


Figure 34. GMEHA flow rate under various frequencies.

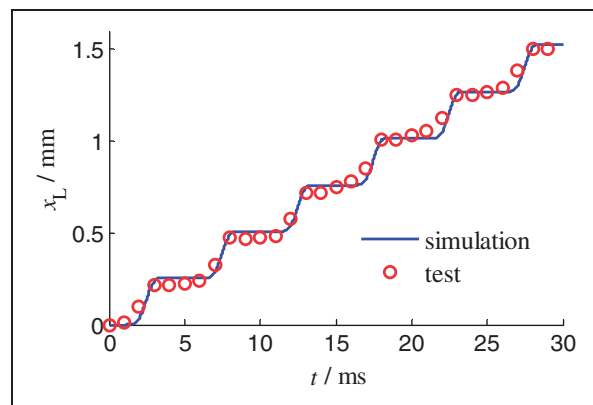


Figure 35. Output displacement of the hydraulic cylinder at 200 Hz.

working principle. Under various excitation frequencies, the GMEHA no-load performance and load performance were tested.

Accordingly, the output displacement of the hydraulic cylinder was measured by a laser displacement sensor to calculate the GMEHA output flow rate; the GMEHA load performance was tested by increasing the weights under the bottom of the hydraulic cylinder output shaft.

The relationship between the GMEHA output flow rate and the excitation frequency with no-load is shown in Figure 34.

As shown in Figure 34, the model results are in good agreement with the experiment data in which the GMEHA optimum working frequency is 250 Hz and the maximum output flow rate with no-load is 0.85 L/min. The GMEHA output flow rate is lower in the low-frequency stage because of the low working frequency. The output flow rate begins to drop over 300 Hz. With the increasing frequency, the backflow phenomenon appears when the valve plate response speed is not higher than the GMEHA driving frequency.

Figures 35 to 38 respectively show the comparison between the model results and the experimental data for the GMEHA hydraulic cylinder output displacement.

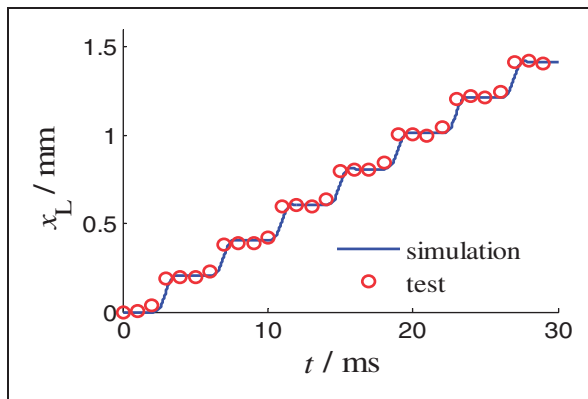


Figure 36. Output displacement of the hydraulic cylinder at 250 Hz.

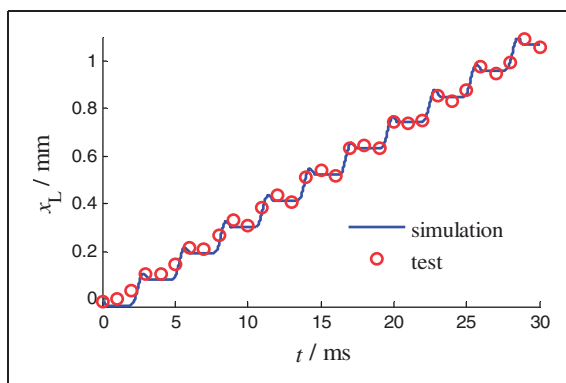


Figure 37. Output displacement of the hydraulic cylinder at 350 Hz.

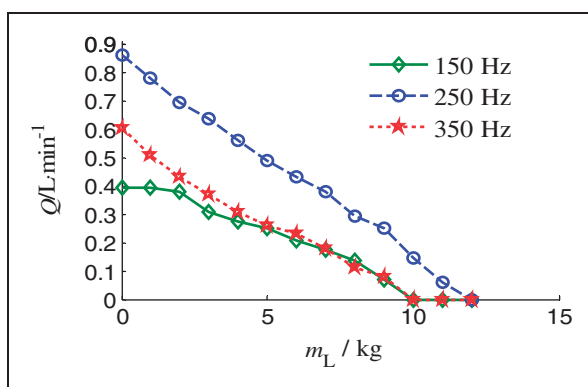


Figure 38. Output flow rate vs output force.

As shown in Figures 35 to 37, the model results show good agreement with the measured experimental data. From the comparison, the backflow phenomenon is not found at 200 Hz and 250 Hz, which indicates that the response speed of the reed valve is higher than the driving frequency. However, when the driving frequency reaches 350 Hz, the backflow phenomenon appears in the experimental data and the model results. Therefore, improving the reed

valve response speed is an important factor to improve the GMEHA output performance.

The load performance of the GMEHA is shown in Figure 38. By comparison, the GMEHA output performance reaches its best at approximately 250 Hz, and the maximum blocked force reaches 120 N. However, the GMEHA output flow decreases with the increase in load.

Conclusions

1. The distribution of the magnetic field within the GMM rod has fine uniformity based on the finite element analysis of the magnetic field when the coil length is close to the length of the GMM rod. The nonuniformity of the axial and radial magnetic field intensity is less than 3% and 0.05%, respectively.
2. Increasing the thickness or reducing the length of the reed valve can improve the valve response speed; however, the valve thickness also increases leading to the increase in the pressure loss.
3. The output flow rate of the GMEHA is limited by the output displacement of the piston in the GMEHA, the opening displacement of the reed valve, and its response speed.
4. The unidirectional performance of the GMEHA is measured at different driving frequencies and operating conditions. The maximum no-load output flow is 0.85 L/min at an approximate driving frequency of 250 Hz, while the blocked force is roughly 120 N.

Declaration of Conflicting Interests

The author(s) declared no potential conflicts of interest with respect to the research, authorship, and/or publication of this article.

Funding

The author(s) disclosed receipt of the following financial support for the research, authorship, and/or publication of this article: This work was supported by the National Natural Science Foundation of China (grant number 51575258), SAST Foundation (2016081), the Fundamental Research Funds for the Central Universities, No.NJ20130013 and sponsored by Qing Lan Project.

References

1. Giurgiutiu V, Chaudhry Z and Rogers CA. Engineering feasibility of induced strain actuators for rotor blade active vibration control. *J Intell Mater Syst Struct* 1995; 6: 583–597.
2. Chaudhuri A. *Self-contained hybrid electro-hydraulic actuators using magnetostrictive and electrostrictive materials*. Thesis, University of Maryland, USA, 2008.
3. Janker P, Claeysen F, Grohmann B, et al. New actuators for aircraft and space applications. In: *The 11th international conference on new actuator*, Bremen(DE), Germany, 2008.

4. Van Den Bossche D. The A380 flight control electro-hydrostatic actuators, achievements and lessons learnt. In: *Proceedings of the 25th congress of the international council of the aeronautical sciences*, Hamburg, Germany, 2006.
5. Larson JP. *Design of a magnetostrictive-hydraulic actuator considering nonlinear system dynamics and fluid-structure coupling*. PhD Thesis, The Ohio State University, USA, 2014.
6. Cloyd JS. Status of the United States Air Force's more electric aircraft initiative. *IEEE Aerosp Electr Syst Magaz* 1998; 13: 17–22.
7. Kim GW and Wang KW. Switching sliding mode force tracking control of piezoelectric-hydraulic pump-based friction element actuation systems for automotive transmissions. *Smart Mater Struct* 2009; 18: 085004.
8. Alfayad S, Ouezdou FB, Namoun F, et al. High performance integrated electro-hydraulic actuator for robotics-part I: Principle, prototype design first experiments. *Sens Actuat A* 2011; 169: 115–123.
9. Provost MJ. The More Electric Aero-engine: A general overview from an engine manufacturer. In: *International conference on power electronics, machines and drives*, UNIV BATH, BATH, ENGLAND, 2002, pp.246–251.
10. Bridger K, Sewell JM, Cooke AV, et al. High-pressure magnetostrictive pump development: A comparison of prototype and modeled performance. In: *Proceedings of SPIE smart structures and materials symposium*, San Diego, CA, USA, 2004, pp.246–257.
11. Anderson EH, Bales GL and White EV. Application of smart material-hydraulic actuators. In: *Smart structures and materials 2003: Industrial and commercial applications of smart structures technologies*, 2003, pp.73–84.
12. Chaudhuri A and Wereley NM. Compact hybrid electrohydraulic actuators using smart materials: A review. *J Intell Mater Syst Struct* 2012; 23: 597–634.
13. Konishi K, Yoshimura T, Hashimoto K, et al. Hydraulic actuators driven by piezoelectric elements (1st report, trial piezoelectric pump and its maximum power). *J Jpn Soc Mech Eng* 1993; 59: 2477–2484.
14. Tang P, Palazzolo A, Kascak A, et al. Combined piezoelectric-hydraulic actuator based active vibration control for rotordynamic system. *J Vib Acoust* 1995; 117: 285–293.
15. Gerver MJ, Goldie JH, Swenbeck JR, et al. Magnetostrictive water pump. In: *Proceedings of SPIE*. vol. 3329: 1998, pp.694–705.
16. Mauck LD and Lynch CS. Piezoelectric hydraulic pump development. *J Intell Mater Syst Struct* 2000; 11: 758–764.
17. Lee DG, Or SW and Carman GP. Design of a piezoelectric-hydraulic pump with active valves. *J Intell Mater Syst Struct* 2004; 15: 107–115.
18. Tan HH, Hurst W and Leo D. Performance modeling of a piezohydraulic actuation system with active valves. *Smart Mater Struct* 2005; 14: 91–110.
19. Rupinsky MJ and Dapino MJ. Smart material electro-hydrostatic actuator for intelligent transportation systems. In: *ASME 2006 international mechanical engineering congress and exposition*, Chicago, Illinois, USA, 5–10 November 2006, pp.721–730.
20. John S, Sirohi J, Wang G, et al. Comparison of piezoelectric, magnetostrictive, and electrostrictive hybrid hydraulic actuators. *J Intell Mater Syst Struct* 2007; 18: 1035–1048.
21. Chaudhuri A, Yoo JH and Wereley NM. Design, test and model of a hybrid magnetostrictive hydraulic actuator. *Smart Mater Struct* 2009; 18: 085019.
22. Kim GW and Wang KW. Enhanced control performance of a piezoelectric-hydraulic pump actuator for automotive transmission shift control. *Proc IMechE, Part D: J Automobile Engineering* 2010; 224: 161–174.
23. Chaudhuri A and Wereley NM. Experimental validation of a hybrid electrostrictive hydraulic actuator analysis. *J Vib Acoust* 2010; 132: 021006.
24. Larson JP and Dapino MJ. Design of a smart material electro-hydraulic actuator with improved frequency bandwidth. In: *Proceedings of SPIE* vol. 834383430K, 2012.
25. Xuan Z, Jin TL, Ha NS, et al. Performance of piezostacks for a piezoelectric hybrid actuator by experiments. *J Intell Mater Syst Struct* 2014; 25: 2212–2220.
26. Cho JH, Goo NS, Xuan Z, et al. Study on flow distribution inside integrated hybrid actuator. *J Mech Sci Technol* 2014; 28: 3583–3588.
27. Zhu YC and Ji L. Theoretical and experimental investigations of the temperature and thermal deformation of a giant magnetostrictive actuator. *Sens Actuat A* 2014; 218: 167–178.
28. Chaudhuri A and Wereley NM. Dynamic model of a hybrid hydraulic actuator utilizing different smart materials. In: *ASME 2007 international mechanical engineering congress and exposition*. New York: American Society of Mechanical Engineers, 2008, pp.193–202.
29. Wang CL. *Research on the nozzle flapper servo valve driven by GMM actuator*. Thesis, Zhejiang University, China, 2005.
30. Wang J, Gong GF and Yang HY. Research and online measurement of bulk modulus of hydraulic oil. *Chinese J Mech Eng* 2009; 45: 120–125.
31. Kim GW. *Design and nonlinear force control of a power-by-wire piezoelectric-hydraulic pump actuator for automotive transmissions*. Thesis, The Pennsylvania State University, USA, 2009.
32. Blevins RD. *Formulas for natural frequency and mode shape*. Malabar, FL: Krieger Publishing Company, 2001.
33. Walters TE. *Development of a smart material electrohydrostatic actuator considering rectification valve dynamics and in situ valve characterization*. Thesis, The Ohio State University, USA, 2008.